

SYNTHETIC BIOLOGY

A sustainable mouse karyotype created by programmed chromosome fusion

Li-Bin Wang^{1,2,3†}, Zhi-Kun Li^{1,2,3†}, Le-Yun Wang^{1,2,3†}, Kai Xu^{1,2,3†}, Tian-Tian Ji^{1,4†}, Yi-Huan Mao^{1,2,3}, Si-Nan Ma^{1,5}, Tao Liu⁶, Cheng-Fang Tu⁶, Qian Zhao⁶, Xu-Ning Fan⁶, Chao Liu^{1,2,3}, Li-Ying Wang¹, You-Jia Shu^{1,4}, Ning Yang^{1,4}, Qi Zhou^{1,2,3*}, Wei Li^{1,2,3*}

Chromosome engineering has been attempted successfully in yeast but remains challenging in higher eukaryotes, including mammals. Here, we report programmed chromosome ligation in mice that resulted in the creation of new karyotypes in the lab. Using haploid embryonic stem cells and gene editing, we fused the two largest mouse chromosomes, chromosomes 1 and 2, and two medium-size chromosomes, chromosomes 4 and 5. Chromatin conformation and stem cell differentiation were minimally affected. However, karyotypes carrying fused chromosomes 1 and 2 resulted in arrested mitosis, polyploidization, and embryonic lethality, whereas a smaller fused chromosome composed of chromosomes 4 and 5 was able to be passed on to homozygous offspring. Our results suggest the feasibility of chromosome-level engineering in mammals.

The laboratory house mouse (*Mus musculus*) has maintained a standard 40-chromosome karyotype after more than 100 years of artificial breeding (1). Over longer time scales, however, karyotype changes caused by chromosome rearrangements are common: Rodents have 3.2 to 3.5 chromosome rearrangements per million years, whereas primates have 1.6 chromosome rearrangements per million years (2). In humans (2n = 46, where n is a single set of chromosomes), the metacentric chromosome 2 was formed by the Robertsonian (Rb) fusion of two acrocentric chromosomes that remain separate in *Gorilla gorilla* (2n = 48) (3). A reciprocal translocation between ancestor human chromosomes 5 and 17 produced chromosomes 4 and 19 in the gorilla (4). Rb fusion or reciprocal translocation can also cause aneuploidy, uniparental disomy, or childhood leukemia (5–7).

Using embryonic stem cells (ESCs) and the Cre-loxP system, researchers have attempted to derive mouse models with programmed chromosome rearrangements, but only subchromosomal rearrangements have been achieved (8). Recent advances in genome editing have greatly facilitated chromosome engineering in haploid yeast (9–11). In mammals, yeast-like haploid ESCs (haESCs) were derived first from unfertilized mouse embryos and then from rat, monkey, and human counterparts (12–16).

However, genomic imprinting is frequently lost in haESCs, limiting their pluripotency and potential for genetic engineering (17–19).

We recently discovered that by deleting three imprinted regions, we could establish a stable sperm-like imprinting pattern in haESCs (20). Because they have yeast-like haploidy and passage-persistent pluripotency, we used these cells in this study to test the feasibility of chromosome engineering in mammals. To ligate the entire arms of two nonhomologous mouse chromosomes into one, we designed a strategy that combined Rb fusion and reciprocal translocation. We wished to address whether we could ligate chromosomes in mammalian cells. We also examined how it would affect stem cell differentiation and chromatin organization and to what extent it would affect mouse phenotypes.

Results

Chromosome ligation in mouse haESCs

We chose to ligate two medium-size mouse chromosomes (chromosomes 4 and 5) head to tail (Chr4+5; Fig. 1A) and the two largest mouse chromosomes (chromosomes 1 and 2) in opposite orientations (Chr1+2 and Chr2+1; Fig. 1A). Telomere and centromere neighboring single-guide RNAs (sgRNAs) with cleavage efficiencies greater than 0.17 were used to generate double-strand breaks (DSBs) in these chromosomes (tables S1 and S2). New haESC lines were established and used before passage 15. After cotransfecting sgRNA- and Cas9-expressing plasmids into haESCs, we used polymerase chain reaction (PCR) to genotype the cells for the desired editing results (table S3). Positive outcomes were identified in 0.69 to 1.4% of transfected cells (fig. S1, A to C). Sanger sequencing analysis revealed bivalent endpoint sequences of targeted chromosomes in which nucleotide deletions and insertions were observed (fig. S1, D to F), indicating interchro-

somal DNA repair by nonhomologous end joining after CRISPR-Cas9-mediated cleavages.

Fluorescence in situ hybridization (FISH) was also used to confirm Chr4+5 and Chr2+1 ligation in haESCs (Chr4+5 haESCs and Chr2+1 haESCs; Fig. 1B). However, Chr1+2 in haESCs (Chr1+2 haESCs) had been split into two. The first part was a segment of chromosome 1 fused with chromosome 2 (Fig. 1B), and the second part was the remaining chromosome 1 fused with an arm of chromosome 17 (fig. S1G), as indicated by standard G-banding karyotype analyses (Fig. 1C). We found ligated chromosomes in karyotype results of replicated experiments as well (fig. S1, H to K). All ligated chromosomes exhibited complete centromere and telomere signals (fig. S2A). We also found microsegments excised from targeted chromosomes that lacked either telomere or centromere signals, except in one Chr4+5 line where a microchromosome that possessed complete centromere and telomere signals was found, indicating a ligation of two microsegments (fig. S2A). All microsegments and microchromosomes disappeared after passage 20.

Continuous sorting has been shown to be required to maintain haploidy and avoid spontaneous diploidization in mammalian haESCs (12–16). After sorting, two Chr4+5 haESC lines, one Chr1+2 haESC line, and two Chr2+1 haESC lines were established. Note that the established Chr1+2 haESC line was one with a split Chr1+2, which indicated that, in comparison to a complete Chr1+2, the split Chr1+2 might be advantageous for the maintenance of haploidy in chromosome-engineered haESCs. Although the appearance and marker-gene expression of engineered haESCs were normal (fig. S2, B and C), DNA content analyses revealed significantly reduced percentages of 1n cells in Chr2+1 haESCs (fig. S2, D and E). Confocal microscopy analysis further revealed the existence of lagging chromosomes that could overlap with one another in dividing Chr2+1 haESCs that maintained haploidy or spontaneously diploidized (fig. S2, F to I). We sorted the cells exhibiting 4n DNA content in each line for ploidy analysis, and those derived from Chr2+1 haESCs showed the highest proportion of authentic polyploidy (24.5%) (fig. S2J).

Hi-C analyses revealed strengthened contacts between ligated chromosomes in engineered haESCs (Fig. 1D and fig. S3, A to C). We also found increased contacts between the split Chr1+2 and chromosome 17 in Chr1+2 haESCs (Fig. 1D). Using this feature, we located the splitting site of Chr1+2 at about 114.3 Mb in chromosome 1, whose proximal arm was fused with chromosome 17 (Chr1+17), thus exhibiting strengthened interchromosomal contacts (fig. S3D). Although the biological function of interchromosomal contacts in animal cells remains unknown (21), these data indicate that they could be strengthened by chromosome

¹State Key Laboratory of Stem Cell and Reproductive Biology, Institute of Zoology, Chinese Academy of Sciences, Beijing 100101, China. ²Institute for Stem Cell and Regeneration, Chinese Academy of Sciences, Beijing 100101, China. ³Beijing Institute for Stem Cell and Regenerative Medicine, Beijing 100101, China. ⁴University of Chinese Academy of Sciences, Beijing 100049, China. ⁵College of Life Science, Northeast Agricultural University, Harbin 150030, China. ⁶Annoroad Gene Technology (Beijing) Co., Ltd., Beijing 100176, China.

*Corresponding author. Email: zhouqi@ioz.ac.cn (Q.Z.); liwei@ioz.ac.cn (W.L.)

†These authors contributed equally to this work.

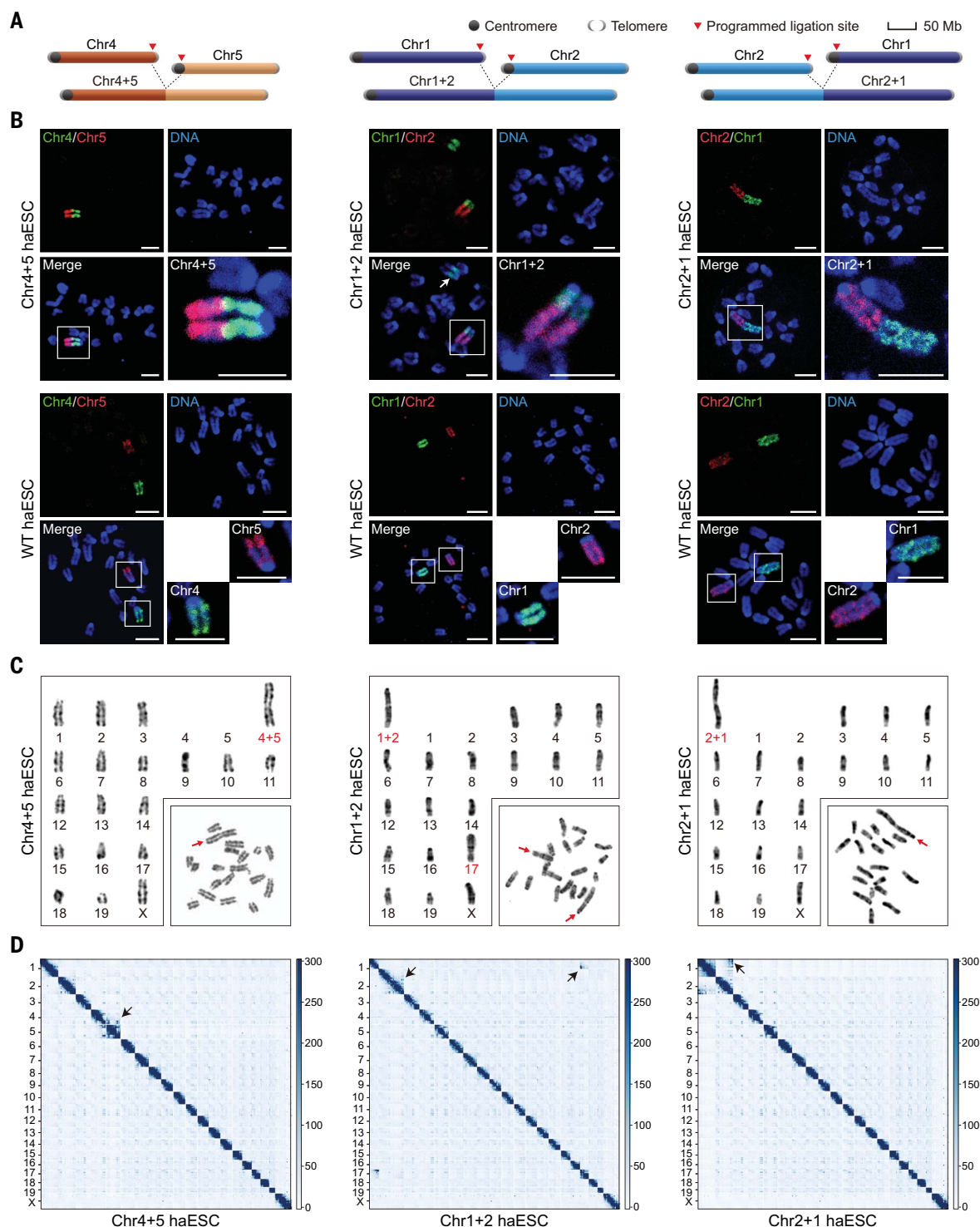


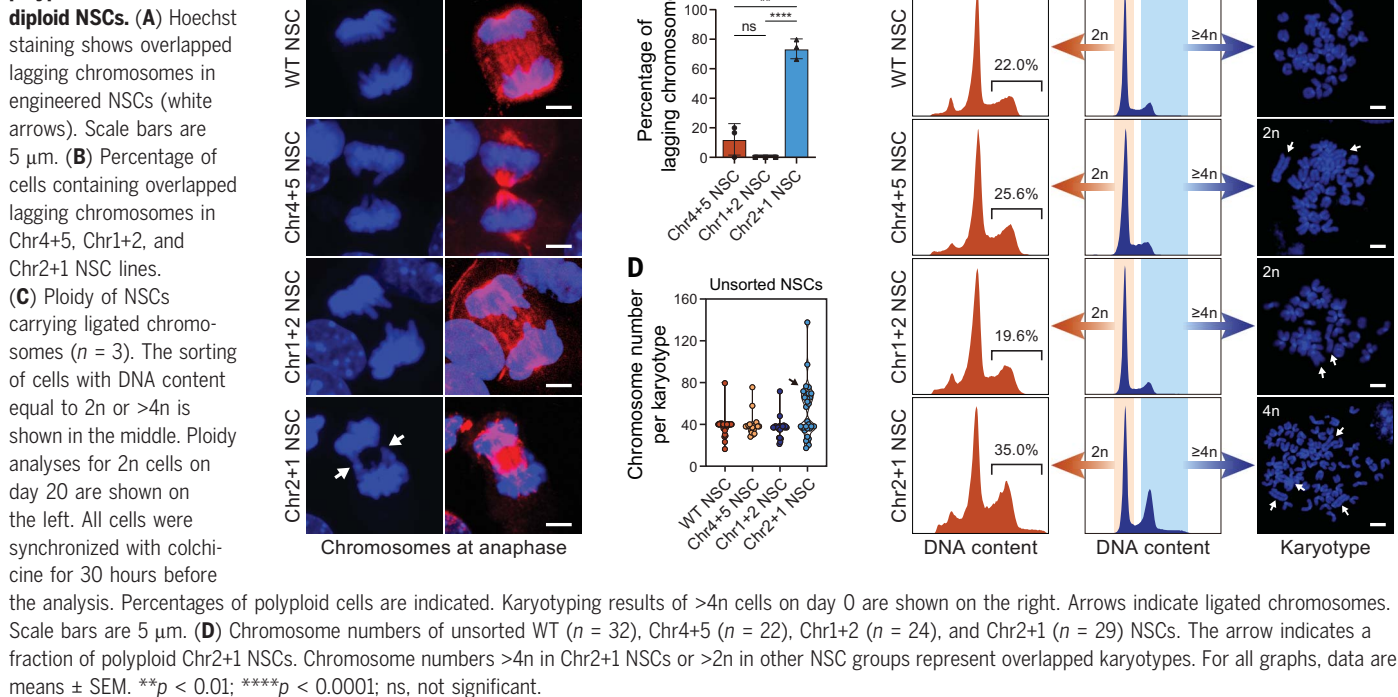
Fig. 1. Engineered chromosome ligation in mouse haESCs. (A) Diagrams for ligation of chromosomes 4 and 5 (Chr4+5), chromosomes 1 and 2 (Chr1+2), and chromosomes 2 and 1 (Chr2+1). (B) FISH detection for ligated chromosomes in Chr4+5 ($n = 10$), Chr1+2 ($n = 6$), and Chr2+1 ($n = 7$) haESCs. The chromosome indicated by an arrow is further illustrated in fig. S1G. WT haESCs ($n = 14$) were used as controls.

Scale bars are 5 μ m. (C) Standard G-banding karyotyping results for Chr4+5, Chr1+2, and Chr2+1 haESCs. Ligated chromosomes are indicated by red arrows and text. (D) Contact maps of Chr4+5 ($n = 2$), Chr1+2 ($n = 2$), and Chr2+1 ($n = 2$) haESCs. Arrows indicate increased interchromosomal contacts. Numbers on the left indicate the chromosome; numbers on the right represent contact values.

ligation. Ligated chromosomes exhibited a limited compartment switch, except chromosome 1 in Chr1+2 haESCs (fig. S3E), on which two opposite compartment switch modes di-

vided by the 114.3-Mb splitting site were identified (fig. S3F). All chromosome-ligated haESCs exhibited transcriptomes similar to those of wild-type (WT) counterparts (fig. S3G).

PacBio sequencing analyses were then used to identify ligations and structural variants (SVs) in each engineered haESC line (fig. S4, A to C). Derived from parallel subclones, Chr1+2

Fig. 2. Ligation-induced polyploidization in diploid NSCs.

haESCs and Chr1+2 haESCs (sc-2; sc, subclone) exhibited identical ligation and distinct SVs (table S4), implying a random occurrence of the latter. Discontinuous reads mapping to 114.3 Mb of chromosome 1 were found in Chr1+2 haESCs and Chr1+2 haESCs (sc-2) and shared a 14-base pair (bp) AT-rich endpoint sequence that indicated the precise splitting site (fig. S4D). Because the 14-bp nucleotides or their neighboring sequences did not match the sequences of sgRNAs, the split likely resulted from random microhomology-mediated end joining, which usually leaves 5- to 25-bp AT-rich endpoint sequences (22). Average SV sizes were 366, 166, and 558 bp in Chr4+5, Chr1+2, and Chr2+1 haESCs, respectively (fig. S4E). No sgRNA targeting site was found near any identified SVs (table S4). Moreover, no correlation between SVs and neighboring gene expression was found in any chromosome-engineered haESC line (fig. S4, F and G).

Mitotic nuclear division arrested by large chromosome ligation

Based on a combination of Hi-C and PacBio sequencing, the arm length was 308.3 Mb for Chr4+5 (156.5 Mb of chromosome 4 plus 151.8 Mb of chromosome 5; fig. S3A), 377.6 Mb for Chr2+1 (182.1 Mb of chromosome 2 plus 195.5 Mb of chromosome 1; fig. S3B), 263.3 Mb for Chr1+2 (81.2 Mb of distal chromosome 1 plus 182.1 Mb of chromosome 2; fig. S3C), and 209.6 Mb for Chr1+17 (114.3 Mb of proximal chromosome 1 plus 95.3 Mb of chromosome 17; fig. S3D). Chr2+1 haESCs exhibited overlapping

lagging chromosomes and a high tendency toward polyploidization. However, the credibility of these observations was compromised by the spontaneous diploidization tendency of haESCs. Following a three-step differentiation procedure (fig. S5A), we tried to obtain diploid neural stem cells (NSCs) from engineered haESCs. Embryoid bodies and NSCs were successively derived and possessed normal appearances (fig. S5B). NSCs also exhibited normal marker-gene expressions, maintained ligated chromosomes, and had a diploid karyotype (fig. S5, B to D). Hi-C results revealed strengthened contacts between ligated chromosomes (fig. S6, A to E). Anaphase lagging chromosomes were found in 12.2, 0, and 73.9% of NSCs carrying Chr4+5, Chr1+2, and Chr2+1, respectively (Fig. 2, A and B). Chr2+1 NSCs exhibited a high tendency toward polyploidization (Fig. 2C). For sorted cells (DNA content $\geq 4n$), only those from Chr2+1 NSCs showed authentic tetraploidy (Fig. 2C). For unsorted cells, Chr2+1 NSCs exhibited a marked polyploidized fraction not found in other groups (Fig. 2D).

Next, we designed a programmed translocation between Chr1+2 and Chr1+17 in Chr1+2 haESCs, aiming to recover full length Chr1+2 (recovered Chr1+2; Fig. 3A). In parallel, we tried to shorten Chr2+1 to the size of Chr1+2 using a programmed translocation with chromosome 17 (truncated Chr2+1 and Chr2+17; Fig. 3A). sgRNAs were designed according to the splitting site (fig. S4D and table S1). As a result, 0.10 to 0.42% of clones were PCR-positive ($n = 4$; table S3). Sanger sequencing and karyotype

analysis confirmed the formation of recovered Chr1+2 (recovered Chr1+2 haESCs) and truncated Chr2+1 and Chr2+17 (truncated Chr2+1 haESCs; fig. S7, A to D).

Spontaneously diploidized ESCs in each haESC line were sorted and labeled with a genome-integrating H2B-RFP-PiggyBac plasmid to show chromosome behavior. Normal nuclear division was observed in 82 WT, 131 Chr4+5, and 56 Chr1+2 ESCs. By contrast, 9 of 112 Chr2+1 ESCs polyploidized during the imaged cycle. We found a continuous existence of overlapped lagging chromosomes in all Chr2+1 ESCs that eventually polyploidized, accompanied by arrested anaphase and refusion of daughter nuclei (Fig. 3B). Although lagging chromosomes were also observed in Chr1+2 and Chr4+5 ESCs at certain time points, they detached from one another with spindle elongation (Fig. 3B). In ESCs that carried recovered Chr1+2, a continuous existence of overlapped lagging chromosomes and refusion of daughter nuclei were found in 8 of 67 observed cells (Fig. 3B). None of 87 ESCs that carried truncated Chr2+1 polyploidized during the imaged cycle (Fig. 3B). These results show that the arm of ligated chromosome Chr2+1 or recovered Chr1+2 (both 377.6 Mb in size) was spatially incompatible for diploid mouse cells, leading to arrested nuclear division and cell polyploidization; shortening the arm size by 114.3 Mb could eliminate this effect.

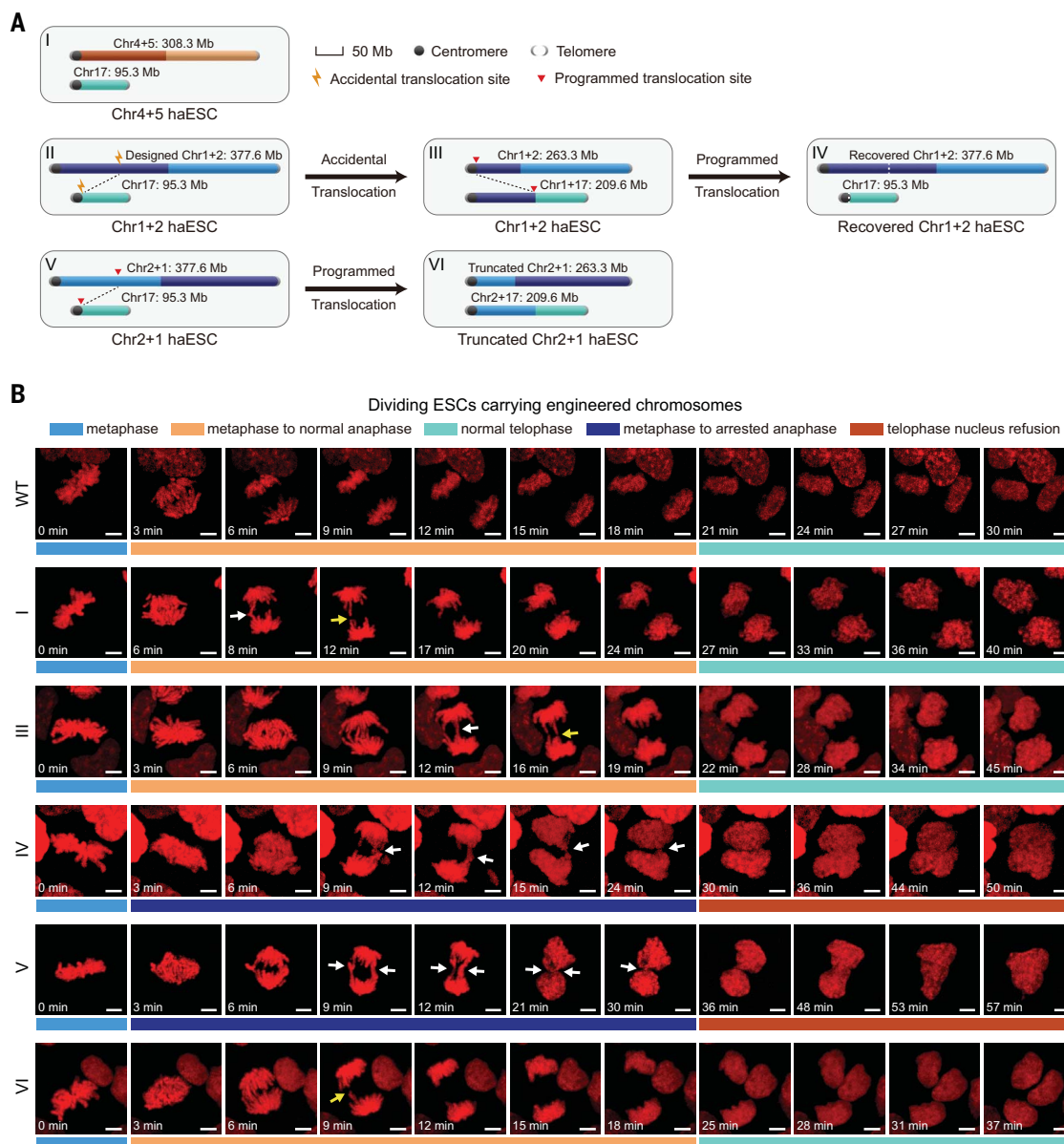
Refusion of daughter nuclei was slower than normal nuclear division (Fig. 3B). Consistent with this observation, we found a lower proliferation

Fig. 3. Cell division is restricted by mouse chromosome engineering. (A) Engineered chromosomes in haESCs:

(I) Chr4+5 and chromosome 17 in Chr4+5 haESCs, (II) Chr1+2 and chromosome 17 in designed Chr1+2 haESCs, (III) Chr1+2 shortened in accidental translocation with chromosome 17 and Chr1+17 formed in the meantime in Chr1+2 haESCs, (IV) recovered Chr1+2 and Chr1+17 in translocated haESCs, (V) Chr2+1 and chromosome 17 in Chr2+1 haESCs, and (VI) truncated Chr2+1 and Chr2+17 forms in the meantime in another translocated haESC.

(B) Continuous nuclear imaging of diploid ESCs: (WT) diploid ESCs with a wild-type karyotype, (I) diploidized ESCs sorted from Chr4+5 haESCs, (III) diploidized ESCs sorted from Chr1+2 haESCs, (IV) diploidized ESCs sorted from recovered Chr1+2 haESCs, (V) diploidized ESCs sorted from Chr2+1 haESCs, and (VI) diploidized ESCs sorted from truncated Chr2+1 haESCs. The time point when all chromosomes are arranged in the equatorial plate (metaphase) is set as 0 min.

White arrows indicate overlapped lagging chromosomes; yellow arrows indicate lagging chromosomes detached by spindle elongation. Scale bars are 5 μ m.



rate in Chr2+1 haESCs (fig. S7E). In truncated Chr2+1 haESCs with normal nuclear division (Fig. 3B), the proliferation rate was recovered (fig. S7E). Sub-G₁ phase proportion analysis indicated that the cell death ratio did not change after the ligations (fig. S7F). Fitted Gaussian curves showed an extended S/G₁ phase in Chr2+1 haESCs (fig. S7G).

Production of viable pups that carry ligated chromosomes

To establish a proper imprinting pattern (20), we deleted three imprinted regions (H19, IG, and Rasgrf1) in engineered haESCs (table S3). Through oocyte injection of derived haESCs, we generated 113 Chr4+5 embryos, 355 Chr1+2 embryos, and 365 Chr2+1 embryos, which were

transferred into surrogate wombs (Fig. 4A). No full-term pup was derived from Chr2+1 embryos, which were abnormal and died before embryonic day 12.5 (E12.5; Fig. 4B and table S5). By contrast, haESC-injected embryos with a WT karyotype achieved full term efficiently (fig. S8A and table S5). Chr2+1 embryos showed a significantly increased percentage of polyploid cells (fig. S8, B to D).

Fourteen and 37 full-term pups were derived from Chr4+5 and Chr1+2 embryos (Chr4+5 and Chr1+2 pups), respectively (Fig. 4B and table S5). Chromosome ligations in these pups were confirmed (Fig. 4C and fig. S8A). Body weights of Chr4+5 (1.37 ± 0.09 g, $n = 13$) and Chr1+2 pups (1.35 ± 0.15 g, $n = 12$) were normal (Fig. 4D) and so were their placenta weights (fig. S8E).

By transferring 68 embryos created by oocyte injection of truncated Chr2+1 haESCs, two full-term living pups were also derived (fig. S8F and table S5).

Ligation-triggered polyploidization was confirmed in haESCs that were diploidized in vitro (Fig. 2) but not in bona fide 2n ESCs derived from mouse embryos. We therefore obtained ESCs from E3.5 Chr4+5, Chr1+2, and Chr2+1 embryos. Four out of 60 ESCs that were derived from Chr2+1 embryos exhibited continuously overlapping chromosomes during the imaged cell cycle, followed by arrested anaphase and nuclear refusion (fig. S8G). All ESCs that were derived from Chr4+5 ($n = 92$), Chr1+2 ($n = 89$), and truncated Chr2+1 ($n = 87$) embryos exhibited normal nuclear divisions (fig. S8G).

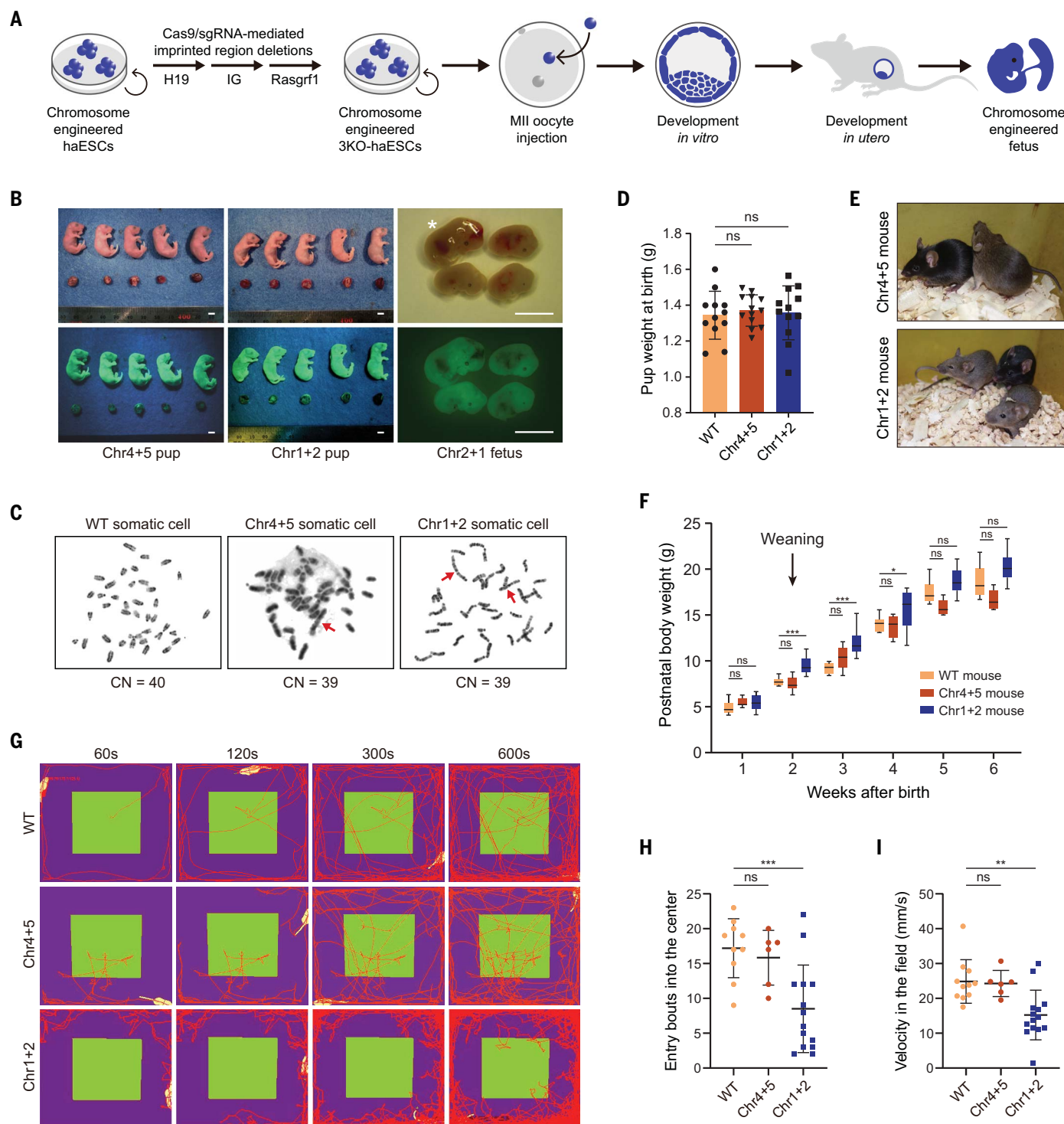


Fig. 4. Production of mice that carry ligated chromosomes. (A) Strategy for generating mouse embryos that carry ligated chromosomes. 3KO, deletions of three imprinted regions; MII, metaphase II. (B) Full-term Chr4+5 and Chr1+2 pups and arrested E12.5 Chr2+1 embryos. Photographs are shown in the top row, and images for green fluorescent protein-positive signals are shown in the bottom row. The embryo with a heartbeat is labeled with an asterisk. Scale bars are 5 mm. (C) Standard G-banding karyotype results. Red arrows indicate ligated chromosomes. CN, chromosome number. (D) Body weights of WT ($n = 12$), Chr4+5 ($n = 13$), and Chr1+2 ($n = 12$) full-term

pups. (E) Adult Chr1+2 (bottom) and Chr4+5 (top) mice. The black mouse is the WT control. (F) Growth curves of WT ($n = 11$), Chr4+5 ($n = 7$), and Chr1+2 ($n = 9$) mice. (G) Activity traces of 8-week-old WT, Chr4+5, and Chr1+2 mice in the open-field test. The time periods along the top indicate 60, 120, 300, and 600 s after the start of test. (H) Entries of WT, Chr4+5, and Chr1+2 mice into the anxiety-provoking central area in the open-field test. (I) Velocities of WT, Chr4+5, and Chr1+2 mice in the open-field test. For all graphs, data are means \pm SEM. * $p < 0.05$; ** $p < 0.01$; *** $p < 0.001$; ns, not significant.

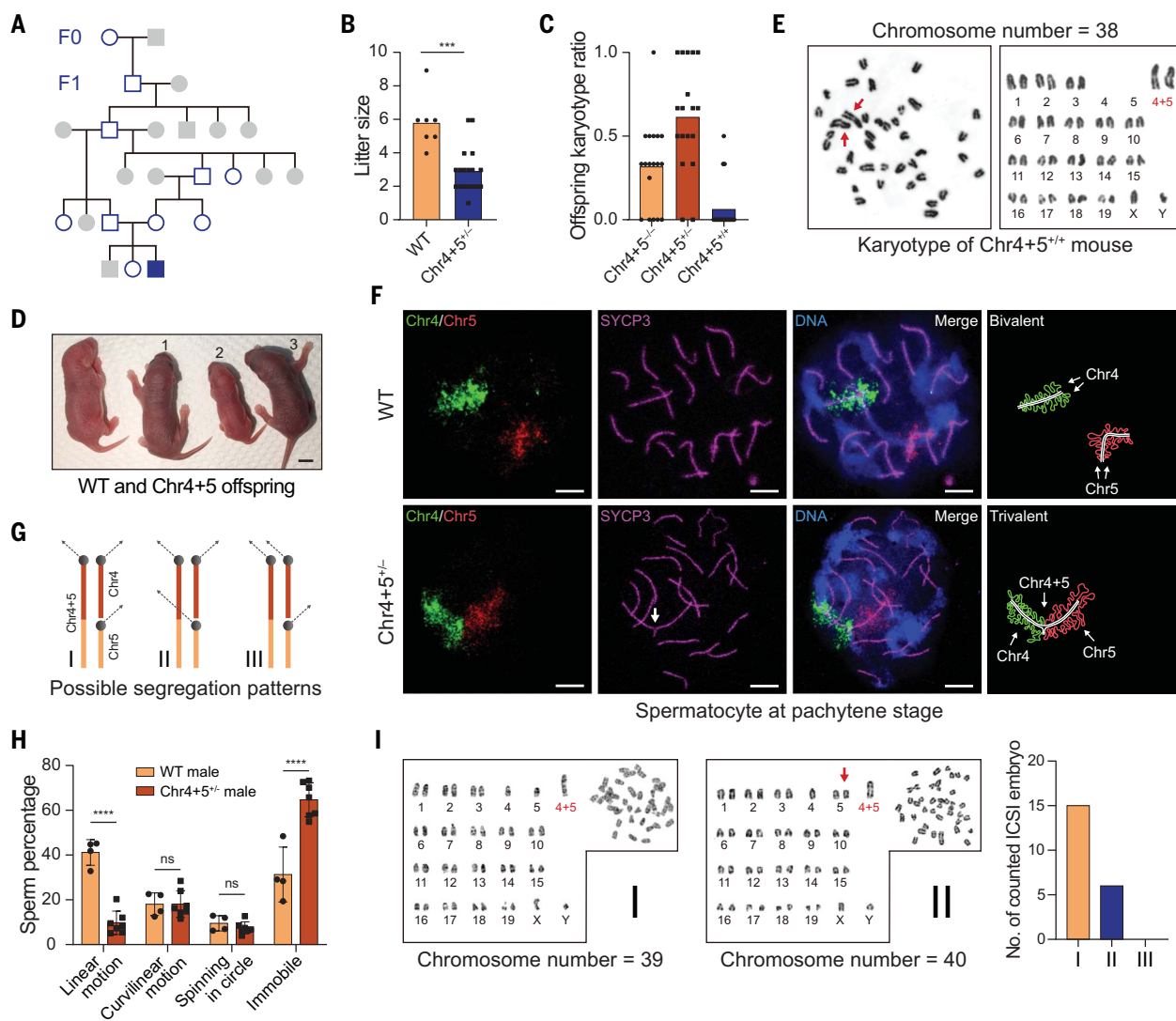


Fig. 5. Deriving homozygous offspring that carry ligated chromosomes.

(A) Deriving a homozygous Chr4+5 offspring in five generations. Square, male; circle, female; open, heterozygous Chr4+5 mice; solid, homozygous Chr4+5 mice; gray, WT mice. (B) Comparison of the litter sizes of Chr4+5^{-/-} mice ($n = 18$) and WT mice ($n = 7$). (C) Ratios of Chr4+5^{-/-}, Chr4+5^{+/-}, and Chr4+5^{+/+} offspring by mating Chr4+5^{+/-} mice ($n = 18$). (D) Female Chr4+5^{-/-} (1), male Chr4+5^{+/-} (2), and male Chr4+5^{+/+} (3) pups. The WT pup is on the left. Scale bar is 5 mm. (E) G-banding karyotyping result of a homozygous Chr4+5 mouse. A pair of Chr4+5 is indicated with red arrows and text. (F) Shown from left to right are FISH detection for chromosomes 4 and 5, chromosome axes indicated

by SYCP3 staining (the Chr4+5-containing axis is indicated by the arrow), merged images with Hoechst-stained DNA, and schemes for trivalent Chr4+5-Chr4-Chr5 and bivalent WT counterparts. Scale bars are 5 μ m. (G) Three hypothetical segregation patterns of trivalent Chr4+5-Chr4-Chr5 in Chr4+5^{+/-} spermatocytes. (H) Comparing sperm mobilities in WT ($n = 4$) and Chr4+5^{+/-} ($n = 7$) mice. (I) Karyotype results for ICSI embryos. Example G-banding karyotypes of ICSI embryos that fit hypothetical segregation patterns I and II are shown on the left and middle. Karyotype distributions of 21 counted ICSI embryos are shown on the right. The red arrow indicates a redundant chromosome 5. For all graphs, data are means \pm SEM. *** $p < 0.001$; **** $p < 0.0001$; ns, not significant.

Chr4+5 and Chr1+2 pups grew to adulthood (Chr4+5 and Chr1+2 mice; Fig. 4E). Chr4+5 mice had normal growth curves, but Chr1+2 mice exhibited overgrowth at weaning (Fig. 4F). In the open-field test for anxiety, Chr4+5 mice entered the center zone at a normal rate, but Chr1+2 mice tended to avoid entering the center zone (Fig. 4, G and H), indicating a high level of anxiety (23). The moving distance and velocity of Chr4+5 mice were normal, whereas Chr1+2 mice moved significantly less and slower (Fig. 4, H and I, and fig. S8, H and I).

Phenotype-associated gene dysregulation in chromosome-ligated mice

We then compared the transcriptomes of the brain, lung, heart, liver, spleen, kidney, and muscle in Chr1+2 mice with those of the WT mice ($n = 2$) and identified 2137 organ-specific and 50 shared differentially expressed genes (DEGs), 26.4% of which were located on chromosomes 1, 2, and 17 (fig. S9, A and B). Chromosome 17, accounting for 3.5% of the genome, had 7.7% organ-specific DEGs and 20% shared DEGs, suggesting a possible correlation between its rearrangement and gene dysregulation. We

analyzed the gene *Capn11*, which encodes a calcium-dependent protease and is located on chromosome 17. It was down-regulated in all organs (fig. S9C). *Capn11* was also down-regulated in *Shank3*-overexpressing mice, a well-characterized model for autism and schizophrenia (24). We therefore tested whether *Capn11* was related to the abnormal behavior of Chr1+2 mice. We deleted *Capn11* in WT C57 mice (*Capn11*^{KO} C57 mice; fig. S10, A to C). The mice avoided the center zone in the open-field test and exhibited increased body weight at weaning (fig. S10, D to F). These data

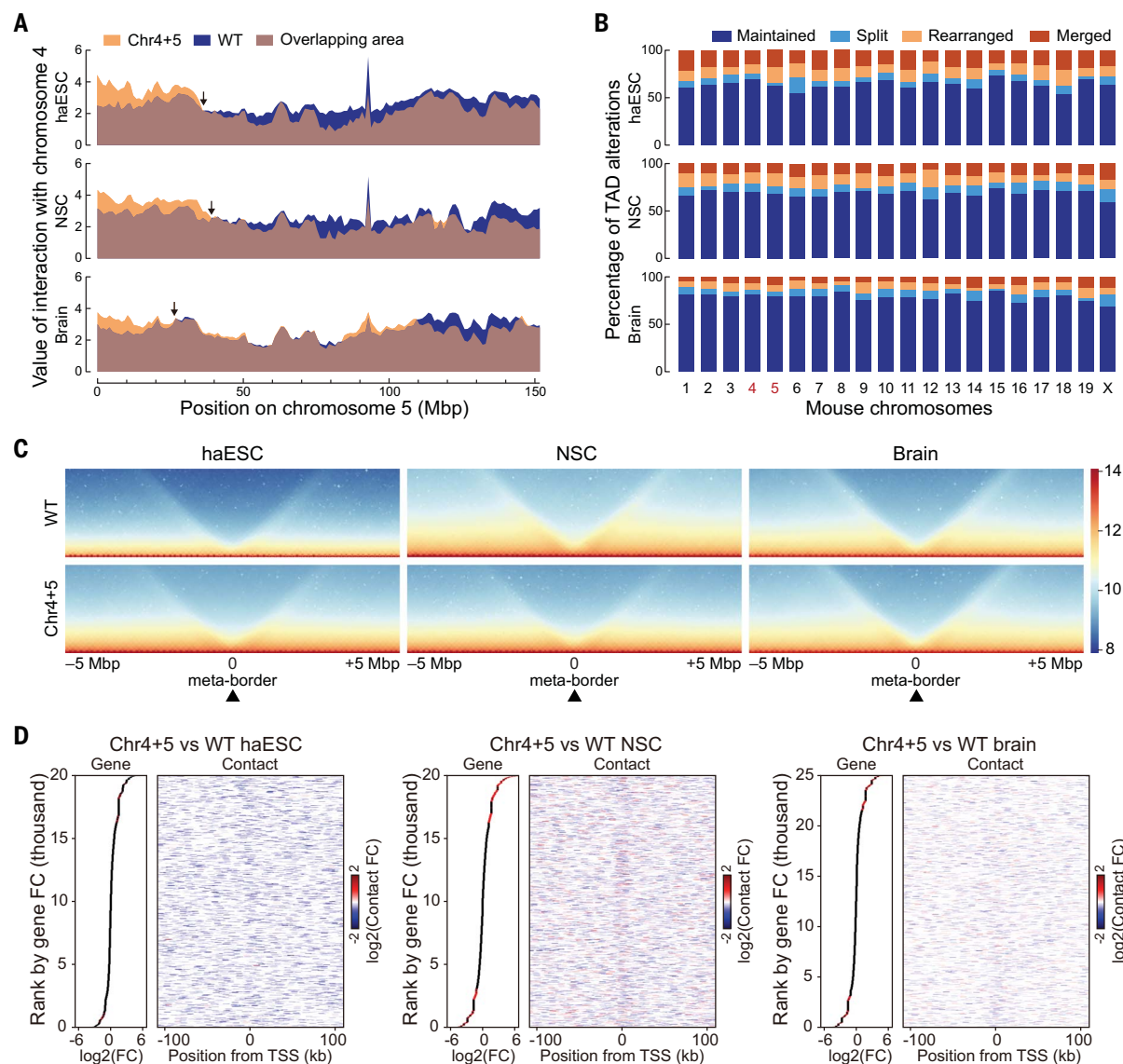


Fig. 6. Chromatin structure disturbances are weakened by differentiation.

(A) Interaction values from chromosome 5 to chromosome 4 in Chr4+5 haESCs, NSCs, and brain. Results for WT haESCs, NSCs, and brain were used as controls. Arrows indicate boundaries for increased interactions. (B) Frequency of TAD alterations between WT and Chr4+5 haESCs, NSCs, and brain. (C) Metaplots for TAD boundaries in Chr4+5 haESCs [mean insulation score (IS) = 2266.48],

NSCs (mean IS = 2255.09), and brain (mean IS = 2254.16). Results for WT haESCs (mean IS = 2061.29), NSCs (mean IS = 2345.57), and brain (mean IS = 2224.56) were used as controls. (D) Combined analyses illustrating altered gene expression and changed chromatin contacts in WT and Chr4+5 haESCs, NSCs, and brain. Genes with an expression fold change (FC) >2 are in red. TSS, transcription start site.

suggested that *Capn11* dysregulation contributed to the behavior phenotype of Chr1+2 mice.

Reduced *Capn11* levels were also found in Chr1+2 haESCs and NSCs (fig. S11A). However, Hi-C analysis revealed no contact change at the *Capn11* locus in these cells (fig. S11B). PacBio sequencing results revealed an intact *Capn11* locus in Chr1+2 haESCs (fig. S11C). ATAC sequencing (assay for transposase-accessible chromatin using sequencing) results also showed no peak pattern change in Chr1+2 haESCs and NSCs (fig. S11D), and virtual 4C analyses revealed no contact pattern change at this locus (fig. S11E). Inferred three-dimensional structure results showed that the normal fold-

ing pattern of chromosome 17 was maintained in Chr1+2 haESCs and NSCs (fig. S11F). A long terminal repeat (LTR) is located within the *Capn11* locus (25), which lacked contact with other genome regions (fig. S11B). Deleting this LTR did not rescue the *Capn11* levels (fig. S11G and H, and table S3). *Capn11* levels were also down-regulated in truncated Chr2+1 haESCs but were restored in Chr2+1 haESCs and even in recovered Chr1+2 haESCs (fig. S11H). Because chromosome 17 was fused with distinct segments in Chr1+2 and truncated Chr2+1 haESCs, these data suggested the existence of a sequence-independent ligation-related effect on *Capn11* dysregulation (26).

Deriving homozygous chromosome-ligated mouse offspring

No pup was derived from mating more than 30 Chr1+2 mice. By contrast, Chr4+5 mice (F_0) produced full-term mice (F_1) after mating with WT mice (Fig. 5A). After multiplying the number of viable embryos (those devoid of H19 and IG deletions) in each litter by four, following the Mendelian ratio, the corrected litter size of F_0 was 2.3 ± 3.1 ($n = 7$), which was significantly lower than that of WT counterparts (5.9 ± 1.6 , $n = 7$; fig. S12A). Of these derived F_1 mice, those carrying ligated chromosomes were identified and confirmed by PCR genotyping, Sanger sequencing, and karyotype analyses

(fig. S12, B to E). Both female and male F_1 mice could transmit Chr4+5 by mating with the WT mice (fig. S12, F and G). We mated female and male heterozygous F_1 mice devoid of all imprinting deletions (Chr4+5 $^{+/-}$ mice), which also exhibited a reduced litter size (2.9 ± 1.8 , $n = 18$; Fig. 5, A and B). Three homozygous mice that carried Chr4+5 (Chr4+5 $^{+/+}$ mice) were derived. They had 19 chromosome pairs (Fig. 5, C to E).

We also derived ESCs from E3.5 Chr4+5 $^{+/+}$ mouse embryos (Chr4+5 $^{+/+}$ ESCs). FISH detection showed that chromosomes 4 and 5 were merged in Chr4+5 $^{+/+}$ ESCs (fig. S13A). By analyzing the organs of Chr4+5 $^{+/+}$ mice, we found merged chromosomes 4 and 5 in all samples by Southern blotting (fig. S13B). Hi-C sequencing results for Chr4+5 $^{+/+}$ mouse brains (Chr4+5 brains) revealed an increase in interchromosomal contacts between chromosomes 4 and 5 (fig. S13C), the levels of which were similar to those of intrachromosomal contacts within native chromosomes (fig. S13D). Together, these data indicated that Chr4+5 was homogeneously retained in the cells and organs of Chr4+5 $^{+/+}$ mice.

A total of 3 Chr4+5 $^{+/+}$ pups, 33 Chr4+5 $^{+/-}$ pups, and 17 WT pups were obtained from 18 litters of Chr4+5 $^{+/-}$ offspring (Fig. 5C). The percentage of Chr4+5 $^{+/+}$ pups (5.7%) was much lower than that of Chr4+5 $^{+/-}$ pups (32.1%) or one half of Chr4+5 $^{+/-}$ pups (62.2%), which did not fit Mendel's law for mating heterozygous parents (+/+; +/-; -/- = 1:2:1). Because Chr4+5 shared homologous sequences with both chromosomes 4 and 5, potential explanations for the mating results could involve errors in pairing or segregation of chromosomes in Chr4+5 $^{+/-}$ germ cells. Using SYCP3 staining to show chromosome axes and FISH detection to indicate chromosomes 4 and 5, we identified separated bivalents of chromosomes 4 and 5 in WT pachytene spermatocytes ($n = 18$) and trivalents that exhibited both signals of chromosomes 4 and 5 in Chr4+5 $^{+/-}$ pachytene spermatocytes ($n = 30$; Fig. 5F), indicating that Chr4+5 can correctly synapse with chromosomes 4 and 5. We therefore propose three hypothetical segregation patterns for paired Chr4+5, Chr4, and Chr5 (Fig. 5G). To dissect the actual segregation outcome, we derived mature sperm from Chr4+5 $^{+/-}$ mice (Chr4+5 $^{+/-}$ sperm; movie S1). The percentage of Chr4+5 $^{+/-}$ sperm that exhibited high mobility (linear motion) was $9.7 \pm 5.2\%$ ($n = 7$), which was lower than that of the WT counterpart ($41.1 \pm 5.8\%$, $n = 4$; Fig. 5H). To avoid bias for highly motile sperm, we used intracytoplasmic sperm injection (ICSI) to generate embryos (ICSI embryos) whose karyotypes could be used to deduce the chromosomal content of the injected sperm. We found embryos with karyotypes consistent with hypothetical segregation pattern I or II but not with segregation pattern III (Fig. 5I).

Chromatin structure changes after engineered chromosome ligation

We found an increased number of contacts between ligated chromosomes in Chr4+5 haESCs, NSCs, and brain (fig. S3A, S6B, and S13D). In Chr4+5 haESCs, increased contacts of chromosome 5 to chromosome 4 were clustered on proximal chromosome 5 (0 to 40 Mb; Fig. 6A), and increased contacts of chromosome 4 to chromosome 5 were clustered on distal chromosome 4 (140 to 160 Mb; fig. S14A). A similar but minor contact change was found in Chr4+5 NSCs, whereas the minimal change was found in Chr4+5 brain (Fig. 6A and fig. S14A). These findings were confirmed by biological replicates that exhibited correlation values ranging from 0.961 to 0.979 (fig. S15A). Topological associated domain (TAD) scores indicated enhanced TAD compactness in Chr4+5 NSCs and brain (fig. S15B). The percentages of changed TADs were 35.8, 31.3, and 21.0% in Chr4+5 haESCs, NSCs, and brain, respectively, exhibiting no prominent distribution on chromosomes 4 and 5 (Fig. 6B and fig. S15C). For those on chromosome 4, changed TADs were randomly scattered across the entire arm (fig. S15D). Meta-TAD borders were strengthened in Chr4+5 haESCs, weakened in Chr4+5 NSCs, and maintained in Chr4+5 brain (Fig. 6C). We identified 58, 1595, and 418 DEGs in Chr4+5 haESCs, NSCs, and brain, respectively, which were not clustered on chromosomes 4 and 5 (fig. S16, A and B). Changed contacts were not clustered at the transcriptional start sites of DEGs (Fig. 6D and fig. S16C). By analyzing genes that were paired by the same changed contacts, we found no correlation between their expression fold changes (fig. S16D). DEGs within changed contacts were enriched in pathways for exocytosis in haESCs, urogenital system development in NSCs, and axonogenesis in brain (fig. S16E).

Discussion

In this study, we created laboratory mouse models that carried chromosome level fusions by engineering. Some engineered mice showed abnormal behavior and postnatal overgrowth, whereas others exhibited decreased fecundity, suggesting that although the change of genetic information was limited, fusion of animal chromosomes could have profound phenotypic effects. *Capn11*, which is located on a rearranged chromosome, might have contributed to the phenotypes. *Capn11* dysregulation could have arisen by means of a sequence-independent effect associated with the rearrangements (26). Changes in TADs and interchromosomal contacts in chromosome-ligated mice were similar to findings with natural Rb mice (27), suggesting that our work could help our understanding of evolutionarily derived chromosome fusions. Ligating the two largest mouse chromosome arms led to

refusion of daughter nuclei, consequently to cell polyploidization, and finally to embryonic lethality, but all of these effects were eliminated when the ligated arms were truncated by two independent translocations. This evidence suggests that the physical space of the mitotic nucleus is a potential constraining factor in mammalian karyotype evolution (28, 29).

Reproductive isolation and formation of new species may arise through accumulating chromosomal rearrangements that reduce fertility in heterozygous hybrids (30, 31). Chr1+2 mice (carrying two rearrangements) did not produce offspring, but Chr4+5 mice (carrying one rearrangement) did, although with limited fecundity. By analyzing the spermatocytes of Chr4+5 mice, we pinpointed the reproduction barrier to a segregation error of ligated chromosomes, which could attribute the reduced fecundity to impaired mobility of aneuploid sperm or the developmental failure of aneuploid embryos. With a lower birth rate, homozygous Chr4+5 mice were derived by mating heterozygous parents, suggesting that one fusion was insufficient for reproductive isolation in mice. Using an imprint-fixed haESC platform and gene editing, we achieved germline-transmittable chromosome ligation in a widely used animal model, the house mouse, which highlights a potential route for large-scale engineering of endogenous or exotic DNA in mammals (32).

REFERENCES AND NOTES

- H. J. Hedrich, *The Laboratory Mouse* (Elsevier, ed. 2, 2012).
- A. Coghlan, E. E. Eichler, S. G. Oliver, A. H. Paterson, L. Stein, *Trends Genet.* **21**, 673–682 (2005).
- Y. Fan, E. Linardopoulou, C. Friedman, E. Williams, B. J. Trask, *Genome Res.* **12**, 1651–1662 (2002).
- P. Stankiewicz, S. S. Park, K. Inoue, J. R. Lupski, *Genome Res.* **11**, 1205–1210 (2001).
- A. Pujol et al., *Reproduction* **131**, 1025–1035 (2006).
- M. F. Greaves, J. Wiemels, *Nat. Rev. Cancer* **3**, 639–649 (2003).
- P. N. Scriven, F. A. Flint, P. R. Braude, C. M. Ogilvie, *Hum. Reprod.* **16**, 2267–2273 (2001).
- Y. Yu, A. Bradley, *Nat. Rev. Genet.* **2**, 780–790 (2001).
- Y. Shao et al., *Nature* **560**, 331–335 (2018).
- J. Luo, X. Sun, B. P. Cormack, J. D. Boeke, *Nature* **560**, 392–396 (2018).
- A. Fleiss et al., *PLoS Genet.* **15**, e1008332 (2019).
- M. Leeb, A. Wutz, *Nature* **479**, 131–134 (2011).
- U. Elling et al., *Cell Stem Cell* **9**, 563–574 (2011).
- I. Sagi et al., *Nature* **532**, 107–111 (2016).
- W. Li et al., *Cell Stem Cell* **14**, 404–414 (2014).
- H. Yang et al., *Cell Res.* **23**, 1187–1200 (2013).
- H. Yang et al., *Cell* **149**, 605–617 (2012).
- W. Li et al., *Nature* **490**, 407–411 (2012).
- H. Wan et al., *Cell Res.* **23**, 1330–1333 (2013).
- Z. K. Li et al., *Cell Stem Cell* **23**, 665–676.e4 (2018).
- P. G. Maass, A. R. Barutcu, C. L. Weiner, J. L. Rinn, *Mol. Cell* **69**, 1039–1045.e3 (2018).
- M. McVey, S. E. Lee, *Trends Genet.* **24**, 529–538 (2008).
- D. Lipkind et al., *J. Appl. Physiol.* **97**, 347–359 (2004).
- C. Jin et al., *Front. Mol. Neurosci.* **11**, 250 (2018).
- A. Sharifi-Zarchi et al., *BMC Genomics* **18**, 964 (2017).
- M. Barbieri et al., *Proc. Natl. Acad. Sci. U.S.A.* **109**, 16173–16178 (2012).
- C. Vara et al., *Nat. Commun.* **12**, 2981 (2021).
- W. Rens, L. Torosantucci, F. Degraasi, M. A. Ferguson-Smith, *Chromosoma* **115**, 481–490 (2006).
- M. A. Ferguson-Smith, V. Trifonov, *Nat. Rev. Genet.* **8**, 950–962 (2007).
- L. H. Rieseberg, *Trends Ecol. Evol.* **16**, 351–358 (2001).

31. J. L. Patton, S. W. Sherwood, *Annu. Rev. Ecol. Syst.* **14**, 139–158 (1983).
32. R. Chari, G. M. Church, *Nat. Rev. Genet.* **18**, 749–760 (2017).

ACKNOWLEDGMENTS

We thank L.-Y. Wei and P.-P. Long from the Institute of Zoology, Chinese Academy of Sciences, for their technical assistance. We thank Q. Meng, X. Yang, X.-L. Zhu, and S.-W. Li from the Institute of Zoology, Chinese Academy of Sciences, for their help with fluorescence-activated cell sorting and confocal laser-scanning microscopy. **Funding:** This work was funded by the Strategic Priority Research Program of Chinese Academy of Sciences XDA16030400 (W.L.); National Key Research and Development Program 2019YFA0110800 and 2019YFA0903800 (W.L.); National Key Research and Development Program 2017YFA0103803 (Q.Zho.); National Key Research and Development Program 2018YFA0108400 (Z.-K.L.); National Natural Science Foundation of China 31621004 (Q.Zho. and W.L.); CAS Project for Young

Scientists in Basic Research YSBR-012 (W.L.); Youth Innovation Promotion Association E229561101 (Z.-K.L.); National Postdoctoral Program for Innovative Talents BX201700243 (Le-Y.W.); and National Postdoctoral Program for Innovative Talents BX20200333 (K.X.). **Author contributions:** Conceptualization: Z.-K.L., L.-B.W., Q.Zho., W.L.; Methodology: L.-B.W., Z.-K.L., Le-Y.W., K.X., T.-T.J., Y.-H.M., S.-N.M., T.L., C.-F.T., Q.Zha., X.-N.F., C.L., Li-Y.W., Y.-J.S., N.Y.; Investigation: L.-B.W., Z.-K.L., Le-Y.W.; Visualization: L.-B.W., Z.-K.L.; Funding acquisition: W.L., Q.Zho., Z.-K.L., Le-Y.W., K.X.; Project administration: W.L., Q.Zho., Z.-K.L., L.-B.W.; Supervision: W.L., Q.Zho.; Writing – original draft: Z.-K.L., L.-B.W.; Writing – review and editing: W.L., Q.Zho., L.-B.W., Z.-K.L. **Competing interests:** The authors declare that they have no competing interests. **Data and materials availability:** All sequencing data generated in this study have been deposited in Genome Sequence Archive of Beijing Institute of Genomics, Chinese Academy of Sciences (<http://gsa.big.ac.cn/>), with the accession number CRA006835. All other data are available in the manuscript or the supplementary materials. **License information:** Copyright © 2022

the authors, some rights reserved; exclusive licensee American Association for the Advancement of Science. No claim to original US government works. <https://www.science.org/about/science-licenses-journal-article-reuse>

SUPPLEMENTARY MATERIALS

science.org/doi/10.1126/science.abm1964

Materials and Methods

Figs. S1 to S16

Tables S1 to S5

References (33–48)

MDAR Reproducibility Checklist

Movie S1

[View/request a protocol for this paper from Bio-protocol.](#)

Submitted 1 September 2021; resubmitted 18 February 2022

Accepted 8 July 2022

10.1126/science.abm1964